



HAL
open science

Sputtered and selenized Sb₂Se₃ thin-film solar cells with open-circuit voltage exceeding 500 mV

G.-X. Liang, Y.-D. Luo, S. Chen, R. Tang, Z.-H. Zheng, X.-J. Li, X.-S. Liu, Y.-K. Liu, Y.-F. Li, X.-Y. Chen, et al.

► To cite this version:

G.-X. Liang, Y.-D. Luo, S. Chen, R. Tang, Z.-H. Zheng, et al.. Sputtered and selenized Sb₂Se₃ thin-film solar cells with open-circuit voltage exceeding 500 mV. *Nano Energy*, 2020, 73, pp.104806. 10.1016/j.nanoen.2020.104806 . hal-02569951

HAL Id: hal-02569951

<https://univ-rennes.hal.science/hal-02569951>

Submitted on 15 Jun 2023

HAL is a multi-disciplinary open access archive for the deposit and dissemination of scientific research documents, whether they are published or not. The documents may come from teaching and research institutions in France or abroad, or from public or private research centers.

L'archive ouverte pluridisciplinaire **HAL**, est destinée au dépôt et à la diffusion de documents scientifiques de niveau recherche, publiés ou non, émanant des établissements d'enseignement et de recherche français ou étrangers, des laboratoires publics ou privés.

Sputtered and selenized Sb₂Se₃ thin-film solar cells with open-circuit voltage exceeding 500 mV

Guang-Xing Liang¹, Yan-Di Luo¹, Shuo Chen^{1*}, Rong Tang¹, Zhuang-Hao Zheng¹, Xue-Jin Li², Xin-Sheng Liu³, Yi-Ke Liu⁴, Ying-Fen Li⁴, Xing-Ye Chen¹, Zheng-Hua Su¹, Xiang-Hua Zhang⁵, Hong-Li Ma⁵, Ping Fan^{1*}

¹*Shenzhen Key Laboratory of Advanced Thin Films and Applications, College of Physics and Optoelectronic Engineering, Shenzhen University, Shenzhen, 518060, P. R China*

²*School of Science and Engineering, The Chinese University of Hong Kong (Shenzhen), Shenzhen, 518060, P. R China.*

³*Key Laboratory for Special Functional Materials of Ministry of Education, Henan University, Kaifeng, 475004, China*

⁴*School of Material and Metallurgical Engineering, Guizhou Institute of Technology, Guiyang 550003, China*

⁵*Univ Rennes, CNRS, ISCR (Institut des Sciences Chimiques de Rennes) UMR 6226, Rennes, F-35000, France*

* Corresponding author,

Email: chensh@szu.edu.cn (Prof. Chen) and fanping@szu.edu.cn (Prof. Fan)

Keywords: Sb₂Se₃ solar cell; Open-circuit voltage; Sputtering; Selenization; Elemental inter-diffusion

Abstract

Antimony selenide (Sb₂Se₃) is a potential absorber material for environment-friendly and cost-efficient photovoltaics and has achieved considerable progress in recent years. However, the severe open-circuit voltage (V_{oc}) deficit ascribed to the interface and/or bulk defect states has become the main obstacle for further efficiency improvement. In this work, Sb₂Se₃ absorber layer was prepared by an effective combination reaction involving sputtered and selenized Sb precursor thin films. The self-assembled growth of Sb₂Se₃ thin films with large crystal grains, benign preferential orientation, and accurate chemical composition were successfully fulfilled under an appropriate thickness of Sb precursor and an optimized selenization scenario.

Substrate structured Sb_2Se_3 thin-film solar cells, a champion device with a power-conversion efficiency of 6.84%, were fabricated. This device is comparable to state-of-the-art ones and represents the highest efficiency of sputtered Sb_2Se_3 solar cells. Importantly, the high V_{oc} of 504 mV is closely related to the reduced deep level defect density for the Sb_2Se_3 absorber layer, the passivated interfacial defects for $\text{Sb}_2\text{Se}_3/\text{CdS}$ heterojunction interface, and the additional heterojunction heat treatment-induced Cd and S inter-diffusion. This significantly improved V_{oc} demonstrates remarkable potential to broaden its scope of applications for Sb_2Se_3 solar cells.

1. Introduction

Solar cells that can directly convert solar energy into electric power show attractive potential to partially replace non-renewable fossil fuels.¹⁻³ Among various generations of photovoltaic devices, thin-film solar cells have been extensively explored due to their advantages of low material consumption, low energy consumption, high power generation, and scalable flexibility.⁴⁻⁷ To date, copper indium gallium selenide (CIGS), cadmium telluride, and perovskites play the leading role with certified power-conversion efficiency (PCE) higher than 22%.⁸⁻¹⁰ However, their natural scarcity, stability, and toxicity are the main concerns resulting in various limitations. Thus, alternative environment-friendly and cost-efficient photovoltaic materials are urgently required and actively investigated. Chalcogenide antimony selenide (Sb_2Se_3) recently emerged as a promising candidate because of its attractive optoelectronic properties, such as a proper bandgap (1.1–1.3 eV, approaching the ideal

Shockley-Queisser value), high absorption coefficient ($>10^5 \text{ cm}^{-1}$), decent carrier mobility ($\sim 10 \text{ cm}^2 \text{ V}^{-1} \text{ s}^{-1}$), and long carrier lifetime ($\sim 60 \text{ ns}$).¹¹⁻¹³ Furthermore, Sb_2Se_3 is a simple binary semiconductor with only one stable orthorhombic crystalline phase; the elemental compositions of Sb and Se also possess the advantages of low toxicity, low cost, and earth abundance. According to theoretical calculations, the PCE of Sb_2Se_3 can reach 30%, further demonstrating its potential as a new photovoltaic absorber layer.¹⁴

Sb_2Se_3 solar cells have been extensively investigated and achieved considerable progress in the last decade, obtaining the current efficiency record of 3.21% for Sb_2Se_3 mesoporous sensitized-type,¹⁵ 7.6% for planar heterojunction geometry-type¹², and the highest 9.2% for core-shell structured Sb_2Se_3 nanorod array solar cells.¹¹ Despite such endeavors, the demonstrated PCE remains far from theoretical predications ($>30\%$). Notably, the key parameters of fill factor (FF) up to 70% and near-unity internal quantum efficiency have already been achieved.¹⁶ However, the open-circuit voltage (V_{oc}) of Sb_2Se_3 solar cell is undoubtedly low with values falling mostly between 0.3 and 0.5 V, implying great space to approach its theoretical thermodynamic limit (0.9 V for E_g equals 1.2 eV).^{6, 16}

The severe V_{oc} deficit ($E_g/q - V_{oc}$) in Sb_2Se_3 solar cells can be attributed to the surface/interface trap states and/or defects/impurities in bulk.³ These defect states can trap photogenerated carriers and accelerate their recombination, leading to the low density of carriers and low V_{oc} . Some experimental surface/interface engineering, such as surface treatment-induced grain boundary inversion,¹⁷ tunable buffer layer,

and double buffer layer optimized band energy alignment,^{18,19} have been conducted as attempts to improve the V_{oc} and PCE of Sb_2Se_3 solar cells. Regarding the defects/impurities belonging to Sb_2Se_3 light absorber layer, high concentration intrinsic point defects (V_{se} and Sb_{Se}) are easy to originate from the thin film preparation process.^{20,21} Various thin film deposition techniques, such as electrochemical deposition,²² solution processing,²³ thermal (or rapid thermal) evaporation,^{24,25} closed-space sublimation (CSS),¹¹ vapor transport deposition (VTD)¹², and magnetron sputtering,²⁶ have been applied to prepare Sb_2Se_3 absorber layer. Thus far, representative Sb_2Se_3 devices with top PCEs have been fabricated by RTE, VTD, and CSS techniques, which can efficiently tune the crystal orientation and crystallinity of Sb_2Se_3 absorber layer to enhance the carrier collection and reduce some recombination loss. By contrast, magnetron sputtering with some advantages, such as full-vacuum operation, precise composition control, excellent uniformity over large areas, and competitive industrial scale-up, is a well-established method that has been extensively used in the preparation of highly efficient CIGS and CZTS solar cells.²⁷⁻²⁹ Therefore, magnetron sputtered Sb_2Se_3 thin films must be further investigated for photovoltaic applications. Recently, our group has reported a substrate structured Sb_2Se_3 thin-film solar cell with an interesting PCE of 6.06%, which was fabricated by magnetron sputtering followed by post-selenization.²⁶ Sb_2Se_3 thin film with benign preferential orientation, accurate chemical composition, and high-quality Sb_2Se_3 /CdS heterojunction interface can be achieved under an optimal selenization scenario. The important V_{oc} of the device is 494 mV, which is superior to

those previously reported efficient Sb_2Se_3 solar cells with the same substrate configuration.^{30,31} Accordingly, further investigation of this effective post-selenization involves magnetron sputtering technique to enable the preparation of Sb_2Se_3 solar cells with enhanced V_{oc} and PCE.

In this work, a modified combination reaction of pre-sputtered and post-selenized Sb metallic precursors for efficient Sb_2Se_3 thin-film solar cells was proposed. The self-assembled growth of Sb_2Se_3 thin films with large crystal grains, benign orientation, and stoichiometric composition has been successfully fulfilled. The thickness of Sb precursor films dramatically influences the quality of Sb_2Se_3 absorber layer and device performance. As a result, the corresponding V_{oc} of our champion device has increased from a value of 494 mV (in our previous work) to 504 mV (in this work). Importantly, a champion device with a highly interesting PCE of 6.84% is comparable to that of state-of-the-art devices and represents the highest efficiency of sputtered Sb_2Se_3 solar cells.

2. Experimental detail

2.1 Deposition of Sb_2Se_3 thin film

Sb metallic precursor thin film was deposited first using radio frequency (RF) magnetron sputtering based on a high-purity and dense Sb sputtering target. A schematic of this preparation process is shown in Fig. 1a. Mo-coated soda lime glass was selected as device substrate, which was ultrasonically cleaned in sequential detergent, acetone, isopropanol, and ethanol solution for 10 min prior to sputtering. The deposition chamber was evacuated to a residual pressure of less than 7.0×10^{-4} Pa

before running the deposition procedures. High-purity argon gas (>99.999%) was introduced at a flow rate of 40 sccm, and the deposition was carried out with a fixed power of 30 W and a relatively low deposition pressure of 0.5 Pa to ensure high compactness. To obtain Sb precursor thin films with different thickness, we controlled the deposition rate (~10 nm/min) and varied the sputtering time from 30 min to 90 min with an increment of 15 min. Subsequently, we implemented an effective post-selenization heat treatment to induce the in-situ combination reaction and self-assembled growth of highly crystalline Sb₂Se₃ thin films. In detail, as shown in Fig. 1b, 0.2 g of high-purity Se powder (99.999%) and the as-deposited Sb thin film were separately placed into a double-chamber vacuum tubular furnace. The chambers were evacuated using a mechanical pump, and argon gas was introduced to thoroughly purge the chambers prior to selenization. A high working pressure of 5×10^4 Pa was applied to provide sufficient Se partial pressure, further passivating the selenium vacancy and obtaining stoichiometric composition. The Se powder side and the Sb precursor thin film side were synchronously heated to 400 °C with a ramping rate of 20 °C/min. After 15 min dwelling, the thin films were naturally cooled down to room temperature.

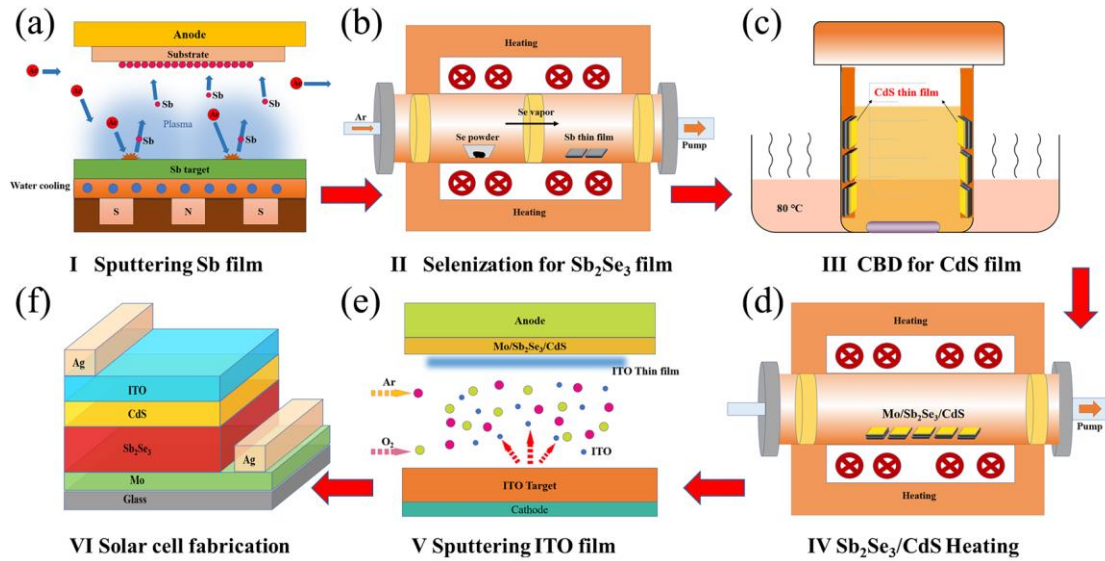


Fig. 1. Schematic illustration of the preparation process of the substrate structured Sb_2Se_3 thin film solar cell. (a) Sb precursor thin film deposited by RF magnetron sputtering, (b) Sb_2Se_3 thin film obtained by post-selenization heat treatment, (c) CdS buffer layer deposited via CBD method, (d) Post-annealing of the $\text{Sb}_2\text{Se}_3/\text{CdS}$ heterojunction, (e) ITO layer deposited by magnetron sputtering, (f) Schematic configuration of the final Sb_2Se_3 thin film solar cell.

2.2 Preparation of Sb_2Se_3 thin film solar cell

After the preparation of Sb_2Se_3 thin film, cadmium sulfide (CdS) buffer layer was then deposited onto the absorber layer via chemical bath deposition (Fig. 1c). Cadmium sulfate ($3\text{CdSO}_4 \cdot 8\text{H}_2\text{O}$) powder, thiourea powder and ammonium hydroxide aqueous solution (28%) were purchased from Aladdin (Shanghai, China). CdSO_4 aqueous solution (0.015 M), thiourea aqueous solution (0.75 M) and ammonium hydroxide aqueous solution were subsequently added to deionized water. The substrates were soaked into the mixed solution which was then placed in a 80 °C water bath under continuous stirring for 9 min. The substrates were rinsed with deionized water and dried in an oven. As shown in Fig. 1d, an additional $\text{Sb}_2\text{Se}_3/\text{CdS}$

heterojunction heat treatment at 300 °C for 5 min in argon atmosphere was designed to induce elemental inter-diffusion and optimize the energy band alignment. Indium tin oxide (ITO) window layer was subsequently deposited using direct current (DC) magnetron sputtering under a power of 60 W, a pressure of 0.4 Pa, and a flow rate of 30 sccm for argon and oxygen gas (Fig. 1e). Finally, the device surface was scribed into small squares with an identical area of 0.15 cm² by a knife. Ag electrodes were thermally evaporated onto the ITO surface to form metallic contact. Fig. 1f shows an as-prepared representative illustration of Sb₂Se₃ thin-film solar cell with the substrate structure of Mo/Sb₂Se₃/CdS/ITO/Ag.

2.3 Characterizations

The crystal structure of Sb and Sb₂Se₃ thin films were characterized by X-ray diffraction (XRD, Ultima-iv) with $CuK\alpha$ radiation under operation conditions of 40 kV and 40 mA. Surface and cross-sectional morphologies of the thin films were observed using a thermal field emission scanning electron microscope (SEM, Zeiss SUPRA 55). A SEM-coupled energy dispersive X-ray spectroscope (EDS, BRUKER QUANTAX 200) was also used to analyze the chemical compositions and elemental distribution. Transmission electron microscopy (TEM) measurements were performed on a FEI Titan Cubed Themis G2 300 microscope. The sample was prepared by ablating a single thin film device by using focused ion beam (FIB, FEI Scios). A Shimadzu UV-3600 UV/Vis/NIR spectrophotometer equipped with monochromator was used for the optical reflectance investigation. Pure soda-lime glass was used as substrate for thin film deposition. Current density-voltage ($J-V$) curves were measured

by using a multi-meter (Keithley, 2400 Series) under AM 1.5G light illumination from a 3A solar simulator with intensity calibrated to 100 mW/cm^2 through a Si reference cell. The voltage was forwardly and backwardly scanned from -0.1 V to 0.6 V with a scan rate of 0.02 V/s . The external quantum efficiency (*EQE*) spectra were obtained using a Zolix SCS101 system with a monochromator and a Keithley 2400 source meter. Electron beam-induced current (EBIC) measurements of the thin film devices were carried out using a Quanta 400 FEG FEI microscope equipped with a Smart EBIC (Gatan, Inc.), the electron-beam voltage and working distance were set as 20 kV and 10 mm , respectively. Capacitance-voltage (*C-V*) measurements were applied at an *AC* amplitude of 30 mV and a frequency of 10 kHz under the dark at room temperature. The DC bias voltage during the *C-V* measurements was applied from -1 V to 0.3 V . Drive level capacitance profiling (*DLCP*) measurements were performed with an *AC* amplitude from 20 mV to 140 mV and a DC bias voltage from -0.2 V to 0.2 V . Temperature-dependent capacitance-frequency measurements were conducted within the frequency range of 1 kHz to 10 MHz . The devices were mounted inside a Janis VPF-100 cryostat and cooled with liquid nitrogen.

3. Results and discussion

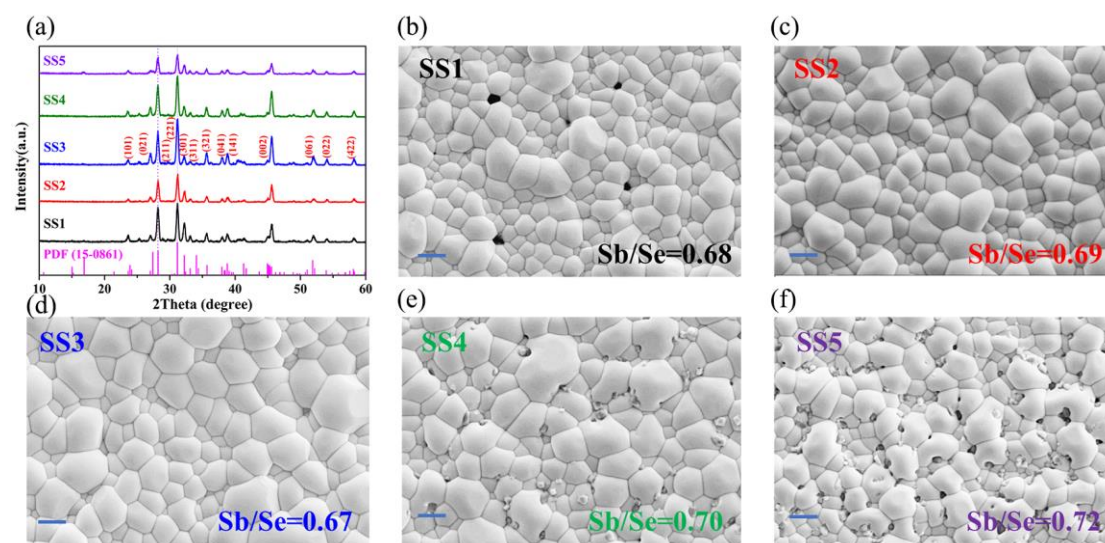


Fig. 2. (a) XRD patterns and (b-f) SEM top-view images of the Sb₂Se₃ thin films with different thickness, labeled as SS1, SS2, SS3, SS4 and SS5, respectively. The blue scale bar at the left bottom corner of each image represents 1 μm.

An appropriate thickness is essential for Sb₂Se₃ solar cells with superior photovoltaic performance. Herein, the Sb₂Se₃ absorber layer with different thicknesses has been obtained by modifying its pristine Sb precursor thin film thickness. Fig. S1 (Supporting Information) shows the XRD patterns and SEM images of the Sb thin films with sputtering times of 30, 45, 60, 75, and 90 min, which are labeled as S1, S2, S3, S4, and S5, respectively. All of the diffraction peaks matched well with the JCPDS standard (No. 35-0732) of the hexagonal phase of metallic Sb. Surface morphologies demonstrated that the Sb thin films consisted of uniform fine grains. The non-compact and blurry boundaries between the grains also imply their non-highly crystalline nature, which can be attributed to the limited mobility and diffusion of Sb atoms under the action of their own energy during the sputtering

process. Afterward, highly crystalline Sb_2Se_3 thin films could be obtained by an additional post-selenization heat treatment. Fig. 2a shows the XRD patterns of the corresponding post-selenized thin films labeled as SS1, SS2, SS3, SS4, and SS5. All of the thin films exhibited prominent peaks in good agreement with the JCPDS standard card (No. 15-0861) of the orthorhombic phase of Sb_2Se_3 without any detectable impurities. Two major diffraction peaks of (211) and (221) show sharp characteristics, indicating its highly crystalline nature, with a preferential crystallographic orientation along (hk1). The obtained Sb_2Se_3 crystal grains growing in vertical direction on the substrate is highly beneficial for reducing interface recombination and absorber transport loss.^{25,32} The top-view SEM images and the Sb/Se ratios of the Sb_2Se_3 thin films with different thickness are also shown in Fig. 2b-f. For SS1 thin film, prominent Sb_2Se_3 crystal grains with clear grain boundaries could be observed, along with distinct pinholes on the sample surface. Since the SS1 sample was quite thin, the selenization time required to fully crystallize the Sb_2Se_3 thin film would be relatively short accordingly. And also because Se has high vapor pressures under elevated temperatures, the pinhole formation could possibly be the result of partial decomposition of the Sb_2Se_3 thin film due to the auxo-action of Se evaporation when an excessive annealing duration was applied to the sample. With increased thickness of Sb thin films, the as-selenized Sb_2Se_3 thin films showed more compact and uniform characteristics, accompanied by the overall growth of the grains with increased average grain size from approximately 450 nm (SS1 thin film) to 850 nm (SS3 thin film). The detailed frequency histograms versus

Sb₂Se₃ grain size distribution are depicted in Fig. S2 (Supporting Information). Moreover, the SS3 thin film had precise Sb/Se ratio close to the standard stoichiometric ratio of 0.67 for Sb₂Se₃. However, if the Sb precursor thin film was too thick, the same post-selenization heat treatment could induce an insufficient selenization or crystallization of Sb₂Se₃, leaving some pristine Sb particles or small Sb₂Se₃ initiative particles on the surface. Notably, a severe stoichiometric deviation belonging to Se-poor further confirmed this observation.

To further investigate the crystalline nature of the as-prepared Sb₂Se₃ thin films, we carried out Raman analysis by using a 514.5 nm laser in the range of 100-300 cm⁻¹. As shown in Fig. 3a, for all of the post-selenized thin films, two major peaks appearing at 190 and 253 cm⁻¹ matched well with the orthorhombic phase of Sb₂Se₃, which could be assigned to the Sb-Se vibration in the Sb₂Se₃ pyramidal unit and the stretching vibrations of Se-Se bond in Se chains, respectively.³³ The reflection spectra of the Sb₂Se₃ thin films were also obtained by UV/Vis/NIR spectrophotometer by using glass as substrate and covering a range of 300–1500 nm. All of the Sb₂Se₃ thin films showed a quite similar short wavelength cut-off edge of approximately 1000 nm (Fig. 3b). A slight variation of reflection value in the absorption region could be attributed to the difference of Sb₂Se₃ grain size and thin film surface roughness. The important information of bandgap (E_g) was calculated using the following formulas:

$$2\alpha d = \ln[(R_{max} - R_{min}) / (R - R_{min})] \quad (1)$$

$$\alpha h\nu = C(h\nu - E_g)^n \quad (2)$$

where α is the absorption coefficient, and d is thickness; the reflectance falls from

R_{max} to R_{min} due to the intrinsic absorption of light by the material.³⁴ The latter is a typical *Tauc* formula, where C is a constant, h is the Planck's constant, ν is the photon frequency, and n is an index defined by 0.5 for direct and 2.0 for indirect bandgap semiconductor.³⁵ The as-selenized Sb_2Se_3 thin films have direct band gaps of 1.174, 1.161, 1.155, 1.148, and 1.144 eV for SS1, SS2, SS3, SS4, and SS5, respectively. Notably, the calculated values agreed well with that given in prior publications for crystalline Sb_2Se_3 thin films.³¹ Moreover, such an optimal bandgap is close to the best value for absorbing efficiently the solar spectrum, making it an attractive candidate for thin film photovoltaic applications.

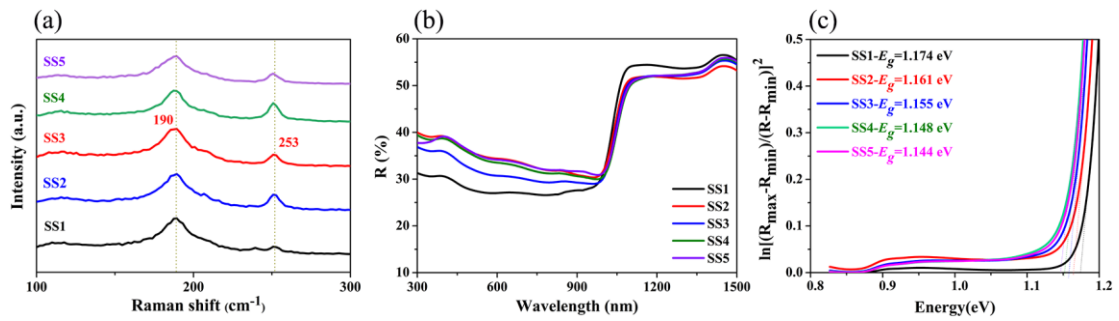


Fig. 3. Optical characterizations of the Sb_2Se_3 thin films with different thickness. (a) Raman spectra, (b) Reflection spectra and (c) Plot of $\ln[(R_{max}-R_{min})/(R-R_{min})]^2$ versus Energy, used to obtain direct band gap.

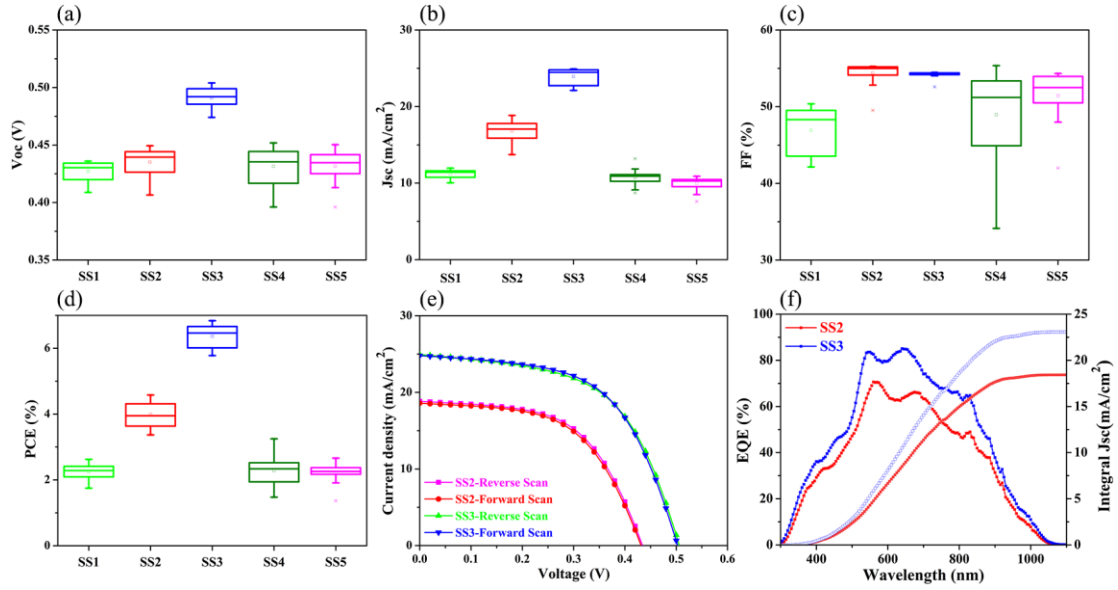


Fig. 4. Performance characterizations of the Sb_2Se_3 thin film solar cells. Statistical distribution of the performance parameters including (a) open-circuit voltage (V_{oc}), (b) short-circuit current density (J_{sc}), (c) fill factor (FF), and (d) power conversion efficiency (PCE). (e) Current density-voltage (J - V) curves of the representative SS2 and SS3 device under forward scan and reverse scan. (f) External quantum efficiency (EQE) and integrated J_{sc} of the devices.

Fig. 4a-d show the statistical distribution of the key device performance parameters, including V_{oc} , short-circuit current density (J_{sc}), FF , and PCE. Thirty-two devices for each sample category (from SS1 to SS5) were fabricated on the basis of their corresponding SS-labeled absorber layer. The acceptable performance variation between the single group devices indicates the good reproducibility of this thin film and device preparation process. The thickness-dependent photovoltaic performance demonstrates the necessity and importance for the Sb_2Se_3 absorber layer with appropriate thickness. XRD and SEM results show that SS3 device with the most superior V_{oc} , J_{sc} , and PCE was closely related to its highly crystalline thin film with

benign preferential orientation, large crystal grains, and standard stoichiometric ratio. These features could effectively reduce the concentration of bulk and interfacial defects, minimize dangling bonds, and suppress recombination loss. The detailed champion device performance parameters of each category are summarized in Table 1.

Table 1. Device performance parameters of the Sb_2Se_3 devices with different thickness

Samples	V_{oc} (mV)	J_{sc} (mA/cm ²)	FF (%)	E_{ff} (%)
SS1	436	11.95	50.37	2.54
SS2	440	18.84	55.25	4.58
SS3	504	24.91	54.47	6.84
SS4	445	13.20	55.35	3.17
SS5	450	10.89	54.30	2.56

The current J - V curves and EQE spectra of the representative SS2 and SS3 thin-film solar cells are shown in Fig. 4e and 4f, respectively. According to the J - V curves, under the simulated AM1.5G solar irradiation, the SS2 device offered a J_{SC} of 18.84 mA/cm², a V_{oc} of 440 mV, and an FF of 55.25%, thus achieving a PCE of 4.58%. In comparison, an obvious improvement of PCE to 6.84% could be observed with the simultaneous improvement of J_{sc} to 24.91 mA/cm² and V_{oc} to 504 mV. Such interesting V_{oc} with a maximum value as high as 504 mV is surpassing the current PCE record of Sb_2Se_3 devices with 400 mV for substrate configuration and 420 mV for superstrate configuration,^{11,12} representing the highest value to that of efficient Sb_2Se_3 thin-film solar cells (Table 2). Moreover, the PCE of 6.84% was also

comparable to that of state-of-the-art devices and represents the highest efficiency of sputtered Sb_2Se_3 solar cells.^{12,26}

Table 2. Comparison of planar heterojunction Sb_2Se_3 solar cells with different fabrication methods

Method	Device configuration	Eff (%)	V_{oc} (mV)	J_{sc} (mA/cm ²)	FF (%)	Ref.
CSS ^{a)}	Mo/ Sb_2Se_3 /Cd _x Zn _{1-x} S/ZnO/AZO	6.71	403	25.69	64.78	Mai [30]
VTD ^{b)}	ITO/CdS/ Sb_2Se_3 /Au	7.60	420	29.90	60.4	Tang [12]
RTE ^{c)}	ITO/CdS/ Sb_2Se_3 /PbS QDs/Au	6.50	427	25.50	59.3	Tang [36]
Co-eva ^{d)}	Mo/ Sb_2Se_3 /CdS/ZnO/AZO/Ag	4.25	427	17.11	58.15	Mai [33]
Sput-Se ^{e)}	Mo/ Sb_2Se_3 /CdS/ITO/Ag	6.06	494	25.91	47.7	Liang [26]
Sput-Sb-Se ^{f)}	Mo/ Sb_2Se_3 /CdS/ITO/Ag	6.84	504	24.91	54.47	This work

^{a)} Closed space sublimation. ^{b)} Vapor transport deposition. ^{c)} Rapid thermal evaporation. ^{d)} Co-evaporation. ^{e)} Sputtering Sb_2Se_3 and post-selenization. ^{f)} Sputtering Sb precursor and post-selenization.

No obvious hysteresis between forward (J_{sc} to V_{oc}) and reverse (V_{oc} to J_{sc}) scans could be observed in our devices (Fig. 4e). This result confirms the high-quality Sb_2Se_3 absorber layer and the reasonable substrate device configuration of Mo/ Sb_2Se_3 /CdS/ITO/Ag. As shown in Fig. 4f, the EQE spectra of the SS2 and SS3 devices exhibited similar broad photo response range from UV to NIR , which overlapped well with the narrow bandgap of Sb_2Se_3 . Importantly, the SS3 device had high quantum response with maximum EQE values higher than 80%. This feature is an important reason accounting for the increase of device, suggesting a less recombination losses at the high-quality Sb_2Se_3 /CdS interface and the passivated bulk absorber layer. The integrated values calculated from EQE data were 18.43 and 23.07 mA/cm² for SS2 and SS3 device, respectively. These values were in close agreement

with the obtained J - V measurement results (Fig. 4e). Importantly, EQE-dependent bandgap values extracted from the inflection point of the EQE spectra in the long-wavelength range were 1.35 and 1.30 eV for SS2 and SS3 absorber layer, respectively.³⁷ An improvement of approximately 0.2 eV relative to its pristine thin film bandgap is reasonable to occur due to the additional $\text{Sb}_2\text{Se}_3/\text{CdS}$ heterojunction heat treatment. The detailed mechanism will be discussed later. Finally, the champion SS3 device was placed in ambient air without any special treatment/encapsulation to investigate its stability. The PCE of the device was measured every 5 days. Only slight performance degradation from the initial 6.84% to the final 6.60% after 60 days storage could be observed (Fig. S3, Supporting Information).

The junction-dependent electrical behaviors of the representative SS2 and SS3 devices were systematically estimated. Dark J - V curves with obvious rectifying characteristics are shown in Fig. 5a. Afterward, device performances, including shunt conductance (G), series resistance (R), diode ideality factor (A), and reverse saturation current density (J_0), were calculated according to the general single exponential diode equation:³⁸

$$J = J_0 \exp \left[\frac{q}{AkT} (V - RJ) \right] + GV - J_L \quad (3)$$

The direct plot of dJ/dV against V is presented in Fig. 5b, where the G values obtained were 5.2 and 1.3 mS/cm^2 for the SS2 and SS3 devices, respectively, by reading from the flat regions under reverse bias. The series resistance R and the diode ideality factor A were obtained by plotting dV/dJ against $(J+J_{SC})^{-1}$ to find the intercept of Y-axis and a slope of AkT/q , respectively (Fig. 5c). For the SS2 device, the linear fitting yielded

an R_{SS2} of $10.76 \Omega \text{ cm}^2$, which then decreased to $2.62 \Omega \text{ cm}^2$ (R_{SS3}) for the SS3 device. The result values of A, the quality factor, were 2.57 and 1.82, implying the more severe interface recombination for SS2 device, whereas the existence of nonuniformity of trap levels in the depletion region at the heterojunction interface for SS3 device. By plotting the $\ln(J+J_{sc}-GV)$ against $V-RJ$ (Fig. 5d), the obtained intercept gave J_0 values of 7.5×10^{-3} and $1.3 \times 10^{-3} \text{ mA/cm}^2$ for SS2 and SS3 device, respectively. Notably, the SS3 device with larger shunt resistance, smaller series resistance and better ideality factor than those of SS2 overall confirmed an improved $\text{Sb}_2\text{Se}_3/\text{CdS}$ heterojunction quality of the device.

The defect states of Sb_2Se_3 were further investigated under dark condition and estimated following the standard space charge limited current model.³⁹ Fig. 5e and 5f show the logarithmic J - V curves of the SS2 and SS3 devices, respectively. In general, the curves can be divided into three regions associated to the exponent n values: the Ohmic region (at low voltages, $n=1$), the trap-filled limit (TFL) region (at intermediate voltages, $n>3$) and the Child region (at high voltages, $n=2$). In the TFL region, the current abruptly increases when the bias voltage exceeds the kink point, demonstrating that the trap states are fully filled by the injected carriers. The obtained onset voltages of TFL region (V_{TFL}) were 0.27 and 0.21 eV for SS2 and SS3, respectively. The trap state density N_{trap} can be calculated by the following relation:⁴⁰

$$N_{trap} = \frac{2\varepsilon\varepsilon_0V_{TFL}}{qL^2} \quad (4)$$

where q is the elementary charge, L is the Sb_2Se_3 thin film thickness, ε_0 is the vacuum permittivity, and ε is the relative dielectric constant (typically 15.1 for Sb_2Se_3).

Compared with the SS2 device, the SS3 device showed a relative lower N_{trap} of $1.29 \times 10^{15} \text{ cm}^{-3}$, which may be attributed to its more superior Sb_2Se_3 thin film quality with less trap sites and reduced defect centers, as corroborated by the SEM images in Fig. 2.

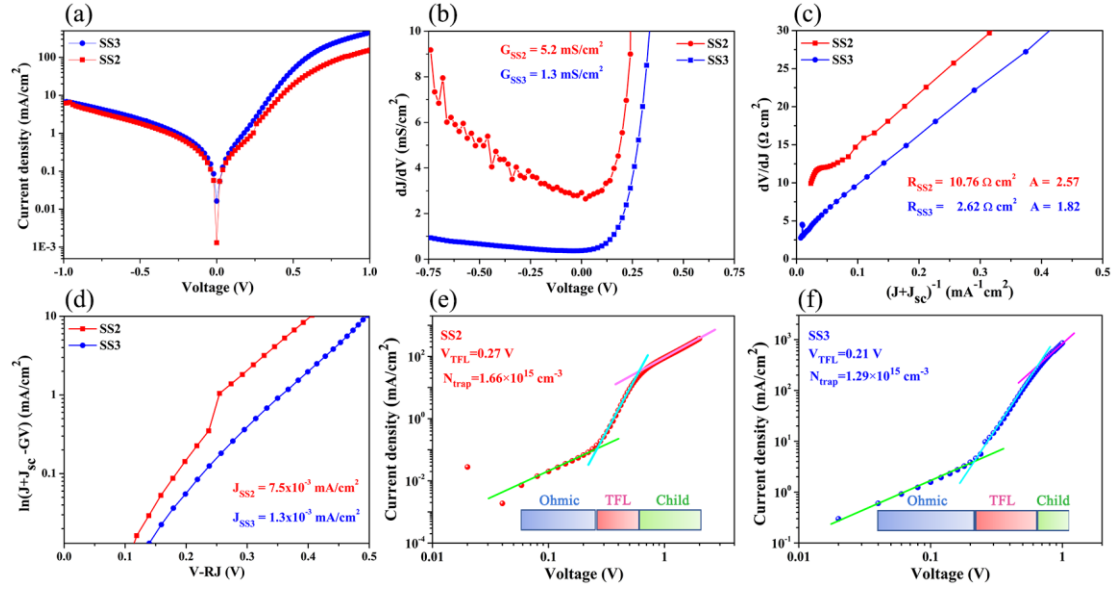


Fig. 5. Electrical behaviors of the representative SS2 and SS3 devices: (a) Dark J - V curves, (b) shunt conductance G characterizations, (c) series resistance R and ideality factor A characterizations, (d) reverse saturation current density J_0 characterizations, (e) and (f) are dark J - V curves of the SS2 and SS3 devices, respectively, showing Ohmic, TFL and Child region.

As mentioned, the obtained V_{oc} (504 mV) is one of the highest values for the state-of-the-art Sb_2Se_3 solar cells. To investigate its improvement mechanism, we first obtained the heterojunction-dependent built-in voltage (V_{bi}) of the representative SS2 and SS3 devices through C - V measurements. Fig. 6a shows the I/C^2 - V curves, from which the value of V_{bi} could be determined by linear fitting and extrapolating to x-axis. V_{bi} of the SS3 device (680 mV) was larger than that of the SS2 device

(637 mV), implying an improved Sb₂Se₃/CdS heterojunction interface for SS3, which was consistent with the above electrical analysis results. Such an interesting V_{bi} belonging to our champion device was also higher than that of many previously reported highly efficient Sb₂Se₃ devices, contributing to an improved V_{oc} in this work.^{14,26} C - V profiling and deep-level capacitance profiling ($DLCP$) characterizations were further carried out to investigate the interfacial defects of the devices (Fig. 6b). In general, the C - V measured doping density (N_{C-V}) includes free carriers, bulk defects, and interfacial defects, whereas the $DLCP$ measured doping density (N_{DLCP}) only represents responses from free carriers and bulk defects.²⁶ Therefore, the interfacial defect density of the device can be calculated by subtracting N_{DLCP} from N_{C-V} . The plots of N_{C-V} and N_{DLCP} against the profiling depth x can be expressed according to the following equations:⁴¹

$$\left\{ \begin{array}{l} N_{C-V} = \frac{-2\varepsilon_{r,n}N_D}{\left(\frac{d(1/C^2)}{dV}\right)qA^2\varepsilon_0\varepsilon_{r,n}\varepsilon_{r,p}N_D + 2\varepsilon_{r,p}} \\ N_{DLCP} = -\frac{C_0^3}{2q\varepsilon_0\varepsilon_{r,p}A^2C_1} \\ x = \varepsilon_0\varepsilon_{r,p}A/C_0 \end{array} \right. \quad (5)$$

where N_D is the doping density of CdS; A is the device area; and ε_0 , $\varepsilon_{r,n}$, and $\varepsilon_{r,p}$ represent the permittivity of free space and the relative permittivity of CdS and Sb₂Se₃, respectively; C_0 and C_1 are two quadratic fitting parameters derived from the C - V curves. The SS2 device showed an evident gap between N_{C-V} and N_{DLCP} curves. By contrast, a small gap between those two curves indicates a low defect density and less recombination loss at the Sb₂Se₃/CdS heterojunction interface for the SS3 device.

This result is closely related to an optimal Sb precursor thin film deposition and post-selenization that produced Sb_2Se_3 thin film with favorable orientation and crystallinity, which can effectively passivate the interfacial defects originated from dangling-bond-rich grain boundaries. In addition, the SS3 device possesses a large depletion width, which is beneficial for the light absorption and carrier extraction ability of the device, corresponding to its much superior device performance.

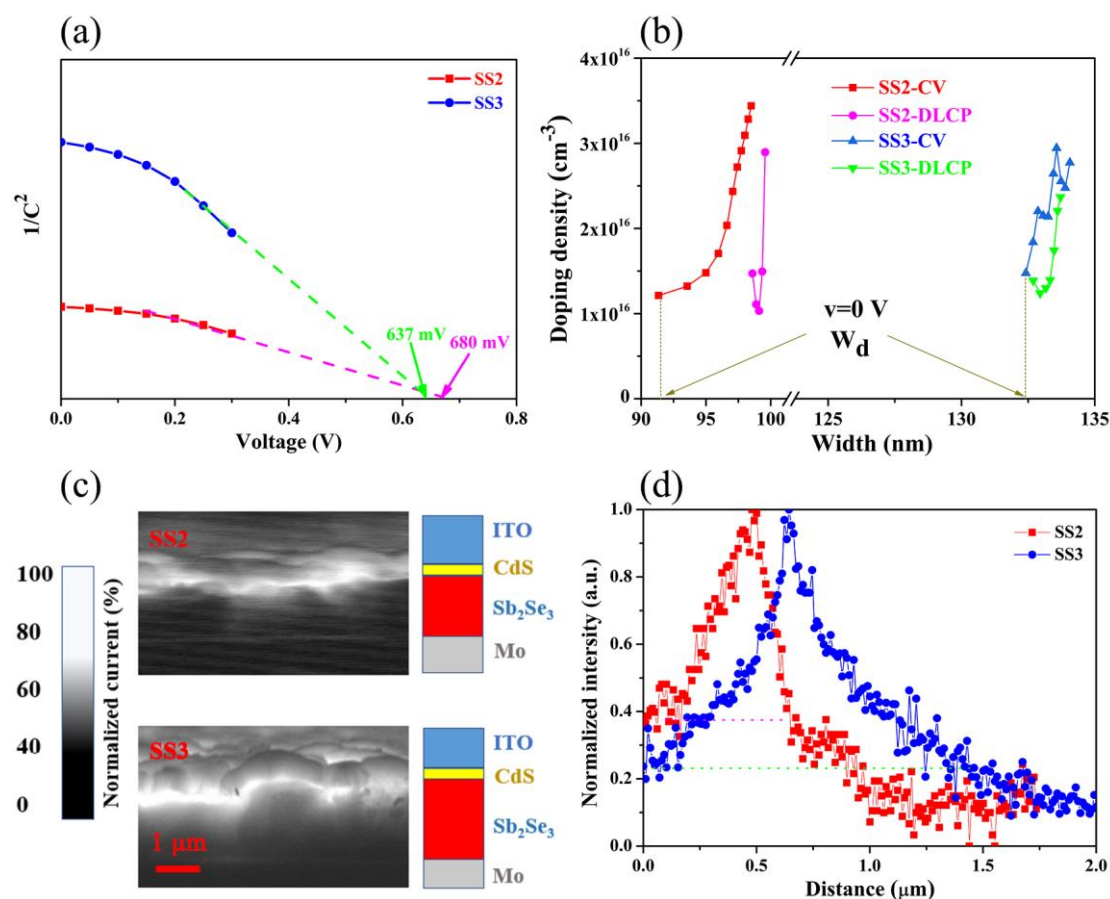


Fig. 6. (a) $1/C^2$ - V plots, (b) CV and $DLCP$ profiles, (c) Cross-sectional EBIC images and (d) EBIC signal intensity profiles of the representative SS2 and SS3 devices.

To further study the depth-dependent carrier collection efficiency of Sb_2Se_3 devices, EBIC measurements were performed, as illustrated in Fig. 6c. The light areas with

high *EBIC* intensity around the $\text{Sb}_2\text{Se}_3/\text{CdS}$ interface can be observed for both devices, indicating high carrier collection efficiency. In comparison, enhanced *EBIC* signals for the SS3 device also indicates less carrier recombination due to effectively reduce of interfacial defects, which is consistent with the *C-V* and *DLCP* analysis results. According to the cross-section distance-dependent normalized electron intensity (zero position corresponds to ITO layer) profile (Fig. 6d), a wide response region matches well with a slightly longer depletion region for the SS3 device, which could be attributed to the lower donor defect density of the sample. The maximum *EBIC* value also showed a right-shift and slow decay rate toward the Sb_2Se_3 absorber layer. Thus, the carrier collection at the deep absorber reveals distinct improvement due to the reduction of the deep defect levels.

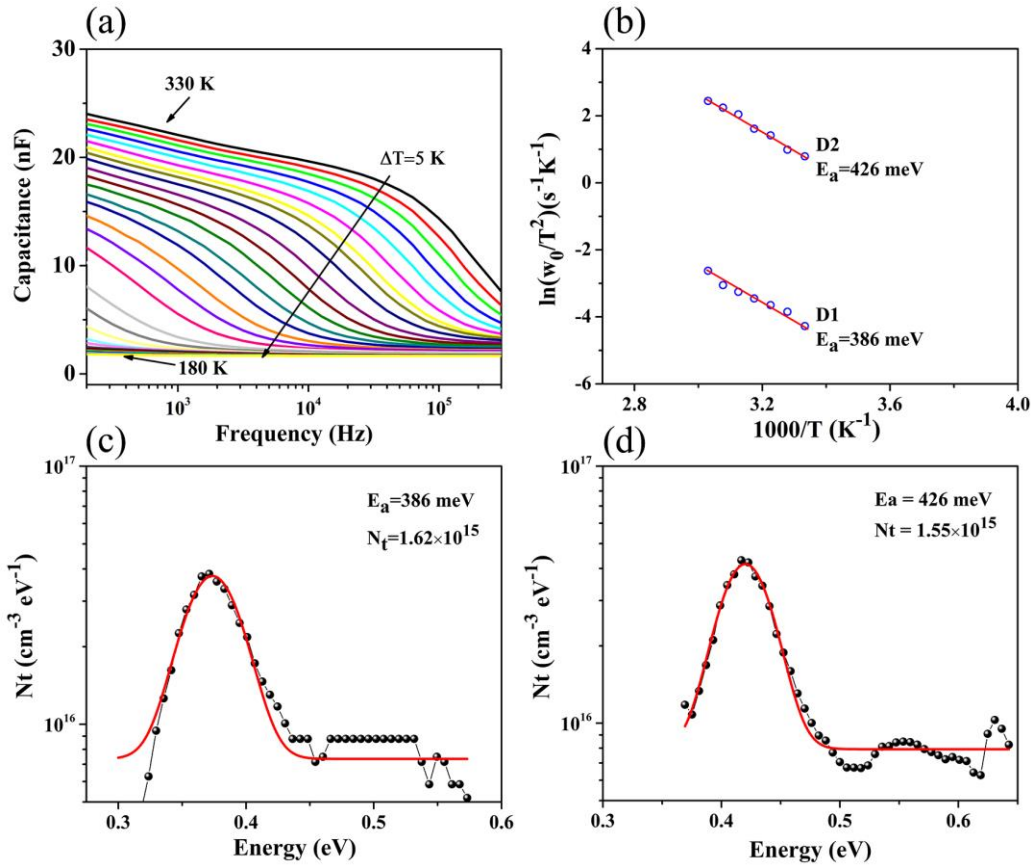


Fig. 7. Temperature-dependent admittance analyses of the champion SS3 device. (a) Capacitance-frequency-temperature (C - f - T) spectra and (b) defect activation energies. Two type defect distributions of $D1$ (c) and $D2$ (d) derived from the admittance spectra.

Admittance spectroscopy was implemented to further understand the distribution and density of defects and defect-induced carrier recombination mechanisms for our Sb_2Se_3 devices. Fig. 7a shows the capacitance-frequency (C - f) spectra of SS3 device measured at various temperatures from 180 K to 330 K with an increment of 5 K. Two capacitance steps were distinguishable with varying frequency, which can be ascribed to two different defect levels denoted as $D1$ and $D2$. The inflection point corresponding to admittance spectrum is determined by the Arrhenius plot. Its frequency value, ω_0 , is derived from the angular frequency point ω at the maximum

of the $\omega dC/d\omega$ plot. The defect activation energies (E_a) were derived from the slopes of the Arrhenius plots that were linearly fitted based on the equation:⁴²

$$\omega_0 = 2\pi\nu_0 T^2 \exp\left(\frac{-E_a}{kT}\right) \quad (6)$$

where ν_0 is the attempt-to-escape frequency, ω_0 is the inflection point frequency, and E_a is the defect activation energy that represents the average energetic depth of the defect relative to the valence band maximum or conduction band minimum. The distribution of each defect type was Gaussian fitted using the Kimerling model based on the following equations:⁴³

$$E(\omega) = kT \ln\left(\frac{2\pi\nu_0 T^2}{\omega}\right) \quad (7)$$

$$N_t(E(\omega)) = -\frac{V_d}{q\omega} \cdot \frac{dC}{d\omega} \cdot \frac{\omega}{kT} \quad (8)$$

where V_d is the built-in potential of the p-n junction, ω is the angular frequency, and $N_t(E(\omega))$ is the defect density. Table 3 presents a summary of defect properties, including the thermal activation energy E_a and the defect density N_t based on temperature-dependent admittance analysis of the representative SS2 (Fig. S4, Supporting Information) and SS3 (Fig. 7) devices. SEM-coupled EDS results (Fig. 2) revealed that the as-prepared Sb_2Se_3 thin films were quite Se deficient. Therefore, donor defects, such as V_{Se} and Sb_{Se} , are prone to form under this scenario. Combined with previously reported first-principle calculation results about the intrinsic defects belonging to Sb_2Se_3 ,²⁰ $D1$ with a low E_a of 386 meV can be ascribed to V_{Se} vacancy defects, whereas $D2$ with E_a of 426 meV can be assigned to Sb_{Se} antisite defects (Fig. 7b). Moreover, for each type of defect, the activation energy difference between

SS2 and SS3 devices is acceptable and follows the *Meyer-Nedel* rule, which illustrates that it should obey the same exponential relationship in different Sb_2Se_3 solar cells.⁴⁴

Table 3. Defect parameters of the SS2 and SS3 devices characterized by admittance spectroscopy

	<i>D1</i>		<i>D2</i>	
	E_a (meV)	N_t (cm^{-3})	E_a (meV)	N_t (cm^{-3})
SS2	310	1.32×10^{16}	407	1.38×10^{16}
SS3	386	1.62×10^{15}	426	1.55×10^{15}

As shown in Table 3, the defect densities of SS3 device are 1.62×10^{15} and $1.55 \times 10^{15} \text{ cm}^{-3}$, respectively, which is almost one order of magnitude less than that of the SS2 device. A large number of deep defects will act as recombination centers, yielding recombination losses both in the Sb_2Se_3 layer and the heterojunction interface, which could significantly deteriorate the device performance. Thus, we can deduce that the SS3 device with high efficiency possesses a low population of donor defects. The deep defects can be effectively passivated under an appropriate thickness of Sb precursor thin film and an optimized selenization scenario during Sb_2Se_3 thin film preparation.

Fig. 8a shows the representative cross-sectional SEM image of the champion SS3 device, which displays an obvious layered structure with approximate thickness of 1280, 80, and 500 nm for Sb_2Se_3 , CdS, and ITO layers, respectively. The Sb_2Se_3 thin film has a significant thickness swelling compared to its initial Sb precursor thin film (~ 600 nm) and is consisted of large crystal grains across the whole layer. It is closely

related to a self-assembled growth mechanism involved with sufficient combination reaction between Sb metallic precursor and Se vapor to form highly crystalline thin film composed of large grains. The interface between Sb_2Se_3 and CdS also shows compact, well-adherent, and pinhole-free characteristics, which is beneficial for reducing charge carrier recombination and current leakage. By contrast, the SS2 device with a Sb_2Se_3 absorber layer thickness of 1050 nm is consistent with its thin Sb precursor thin film. An observable fracture zone between $\text{Sb}_2\text{Se}_3/\text{CdS}$ heterojunction interface could result an unsatisfactory device performance (Fig. S5, Supporting Information). Furthermore, the corresponding EDS elemental mappings marked with Mo, Se, Sb, Cd, In, Sn, O, and S were also conducted to investigate the compositional distribution. Sb and Se present good compactness and uniformity throughout the entire Sb_2Se_3 absorber layer, confirming the high quality of this as-prepared Sb_2Se_3 thin film. Notably, an observable Cd and S inter-diffusion is reasonable to occur because of the additional post-annealing of the $\text{Sb}_2\text{Se}_3/\text{CdS}$. Such an important heterojunction heat treatment yields a champion $\text{Cu}_2\text{ZnSnS}_4$ photovoltaic device by constructing additional favorable band alignments and reducing non-radiative recombination loss.²⁹ Accordingly, the Cd and S inter-diffusion to absorber layer could modify the bandgap of Sb_2Se_3 , increase its doping concentration, reduce the corresponding bulk recombination, and therefore improve the V_{oc} and PCE of the device.

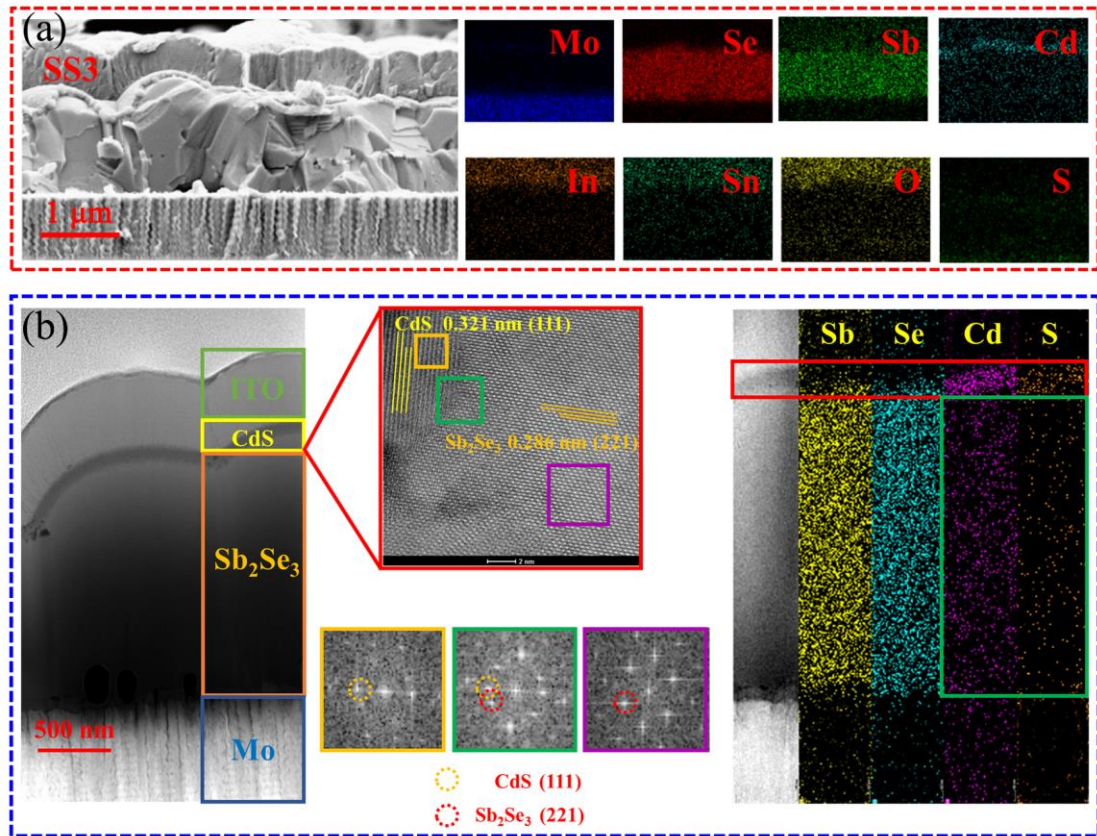


Fig. 8. Morphological and structural characterizations of the champion SS3 device. (a) Cross-sectional SEM image of the device and the corresponding EDS elemental mappings of Mo, Se, Sb, Cd, S, O, Sn and In, used to reveal the compositional distribution. (b) Cross-sectional TEM image of the device, HRTEM image and the selected area Fast Fourier Transform (FFT) patterns as well as the corresponding EDS elemental mappings of Sb₂Se₃/CdS heterojunction interface.

To further investigate the Sb₂Se₃/CdS heterojunction interface as well as the diffusion mechanism, we performed morphological and structural characterizations of the champion SS3 device by TEM, as shown in Fig. 8b. The existence of layered structure with specific thickness was consistent with SEM results (Fig. 8a). High-resolution TEM analysis was implemented at the Sb₂Se₃/CdS interface. The CdS (111) plane shows clear lattice fringe with 0.321 nm interplanar d-spacing, whereas the lattice

fringe with interplanar d-spacing of approximately 0.286 nm matches well with the distance of the (221) lattice plane of the orthorhombic phase Sb_2Se_3 . Though it is not exactly epitaxial growth of CdS on the Sb_2Se_3 layer due to lattice mismatch, an obvious interface with smooth and adherent contact could be observed. The absence of crystal lattice distortion, dislocation, or amorphous layer at the interface region further demonstrates its efficient generation and separation of photocarriers. The electron diffraction patterns of $\text{Sb}_2\text{Se}_3/\text{CdS}$ interface (green area), Sb_2Se_3 side (purple area), and CdS side (yellow area) by Fourier transform are also shown in Fig. 8b. The diffraction spots of the CdS (111) and Sb_2Se_3 (221) planes showed close nature, implying its favorable carrier extraction and suppressible interface recombination for obtaining efficient solar cells. The TEM-coupled EDS mapping results (Fig. 8b) demonstrated the positive MoSe_2 interfacial layer with less than 50 nm was much thinner than that of the Sb_2Se_3 solar cells with ~ 200 nm in our previous work²⁶, which may due to the Se vapor would preferentially react with the Sb precursor than with Mo substrate, thus limiting the MoSe_2 thickness in the selenization process. Notably, an evident inter-diffusion of Cd and S to the Sb_2Se_3 absorber layer was further confirmed.

A schematic of the $\text{Sb}_2\text{Se}_3/\text{CdS}$ heterojunction heat treatment-induced elemental inter-diffusion is shown in Fig. 9a. As mentioned, the Cd and S were assured to diffuse into the Sb_2Se_3 absorber layer, resulting in increased doping concentration to partially improve the V_{oc} of the device. In addition, such an interesting elemental diffusion could also modify the energy-level alignment of the device (Fig. 9b). Cd

possesses fewer valence electron than Sb, thus replacing Sb with Cd constitutes hole doping (P-type). Moreover, the Se atoms partially replaced by S atoms could also result in a slightly enlarged bandgap from the initial E_{g1} to the final E_{g2} , which was also consistent with the absorption spectrum and EQE spectrum determined bandgap results. In summary, the obtained built-in voltage V_{bi} of the Sb_2Se_3/CdS heterojunction markedly increased. The above C-V measurement determined V_{bi} with a maximum value of 680 mV is higher than that of some state-of-the-art devices, which undoubtedly accounts for the highly interesting V_{oc} in this work.

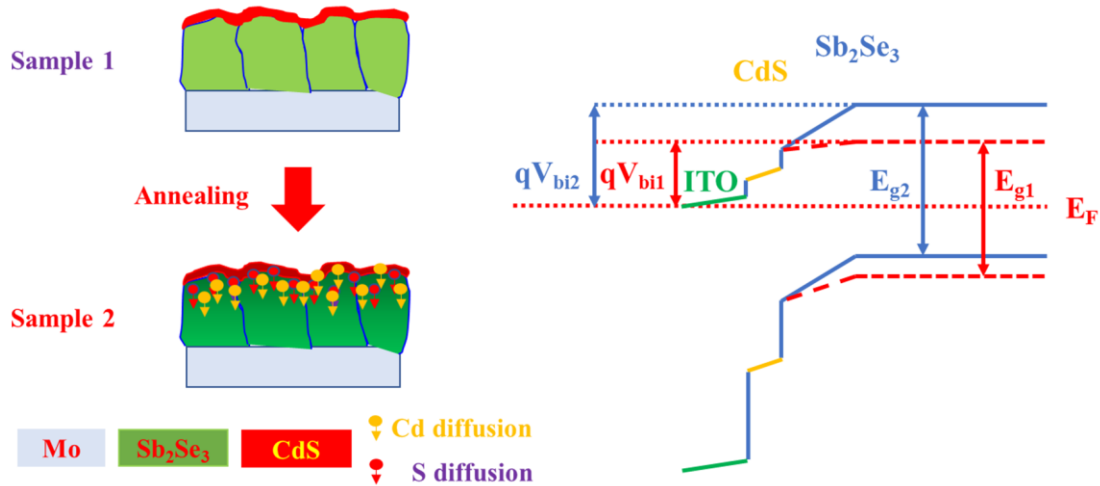


Fig. 9. (a) A schematic diagram of the post-annealing induced elemental inter-diffusion of Cd and S. (b) The modified energy-level alignment of the device.

3. Conclusion

In this work, Sb_2Se_3 absorbing thin films with different thickness were prepared via an effective combination reaction of selenizing pre-sputtered Sb metallic precursors under Se vapor. Sb_2Se_3 thin films with micro-size crystal grains, (hkl) preferential orientation, and standard stoichiometric composition could be obtained under an

appropriate thickness of Sb precursor and an optimized selenization scenario. Sb_2Se_3 thin-film solar cells with a substrate structure of $\text{Mo}/\text{Sb}_2\text{Se}_3/\text{CdS}/\text{ITO}/\text{Ag}$ were fabricated, and the absorber layer thickness-dependent photovoltaic performance demonstrated its necessity and importance. A champion device with a PCE of 6.84% is comparable to state-of-the-art devices and represents the highest efficiency of sputtered Sb_2Se_3 solar cells. Importantly, a highly interesting V_{oc} of 504 mV greatly surpasses that of Sb_2Se_3 solar cells with top PCEs. A systematic investigation of junction-dependent electrical behaviors, depth-dependent carrier collection, and distribution/density of defects and a detailed morphological and structural characterization of $\text{Sb}_2\text{Se}_3/\text{CdS}$ heterojunction interface revealed the improvement mechanism of V_{oc} . Specifically, the mechanism includes passivated interfacial defects, reduced bulk defect density, increased elemental inter-diffusion induced doping concentration, and energy-level alignment modification. These interesting results can pave the way for further enhancing the V_{oc} and PCE of Sb_2Se_3 solar cells.

Acknowledgements

This work was supported by Key Project of Department of Education of Guangdong Province (No. 2018KZDXM059) China, Science and Technology plan project of Shenzhen (JCYJ20190808153409238) China, Natural Science Foundation of Guangdong Province (2020A1515010805) China, National Natural Science Foundation of China (No. 61404086, U1813207, 51802050, U1804160) China, The Natural Science Foundation of Guizhou Province (Qian Ke He [2017] 1064) China, The postgraduate innovation development fund project of Shenzhen University (PIDFP-ZR2019019) China, Shenzhen Key Lab Fund (ZDSYS 20170228105421966) China. The authors wish to acknowledge the assistance on HAADF-STEM observation received from the Electron Microscope Center of the Shenzhen University.

References

- [1] A. Hussain, S. M. Arif, M. Aslam, Emerging renewable and sustainable energy technologies: State of the art. *Renewable Sustainable Energy Rev.* 2017, 71, 12-28.
- [2] R. L. Fares, M. E. Webber, The impacts of storing solar energy in the home to reduce reliance on the utility. *Nat. Energy* 2017, 2, 17001.
- [3] H. Lei, J. Chen, Z. Tan, G. Fang, Review of Recent Progress in Antimony Chalcogenide-Based Solar Cells: Materials and Devices. *Solar RRL* 2019, 3, 1900026.
- [4] D. J. Xue, S. C. Liu, C. M. Dai, S. Chen, C. He, L. Zhao, J. S. Hu, L. J. Wan, GeSe Thin-Film Solar Cells Fabricated by Self-Regulated Rapid Thermal Sublimation. *J. Am. Chem. Soc.* 2017, 139, 958-965.
- [5] B. Liu, L. Bai, T. Li, C. Wei, B. Li, Q. Huang, D. Zhang, G. Wang, Y. Zhao, X. Zhang, High efficiency and high open-circuit voltage quadruple-junction silicon thin film solar cells for future electronic applications. *Energy Environ. Sci.* 2017, 10, 1134-1141.
- [6] W. Wang, X. Wang, G. Chen, L. Yao, X. Huang, T. Chen, C. Zhu, S. Chen, Z. Huang, Y. Zhang, Over 6% Certified $\text{Sb}_2(\text{S},\text{Se})_3$ Solar Cells Fabricated via In Situ Hydrothermal Growth and Postselenization. *Adv. Electron. Mater.* 2019, 5, 1800683.
- [7] S. Chen, Z. Zheng, M. Cathelinaud, H. Ma, X. Qiao, Z. Su, P. Fan, G. Liang, X. Fan, X. Zhang, Magnetron sputtered Sb_2Se_3 -based thin films towards high performance quasi-homojunction thin film solar cells. *Sol. Energy Mater. Sol. Cells* 2019, 203, 110154.
- [8] R. Carron, S. Nishiwaki, T. Feurer, R. Hertwig, E. Avancini, J. Lockinger, S. C. Yang, S. Buecheler, A. N. Tiwari, Advanced Alkali Treatments for High-Efficiency $\text{Cu}(\text{In},\text{Ga})\text{Se}_2$ Solar Cells on Flexible Substrates. *Adv. Energy Mater.* 2019, 9, 1900408.
- [9] M. A. Green, E. D. Dunlop, D. H. Levi, J. Hohl-Ebinger, M. Yoshita, Ho-Baillie, A. W. Y., Solar cell efficiency tables (Version 55). *Prog. Photovoltaics* 2020, 28, 3-15.
- [10] M. Stolterfoht, V. M. Le Corre, M. Feuerstein, P. Caprioglio, L. J. A. Koster, D. Neher, Voltage-Dependent Photoluminescence and How It Correlates with the Fill Factor and Open-Circuit Voltage in Perovskite Solar Cells. *ACS Energy Lett.* 2019, 4, 2887-2892.
- [11] Z. Li, X. Liang, G. Li, H. Liu, H. Zhang, J. Guo, J. Chen, K. Shen, X. San, W. Yu, R. E. I. Schropp, Y. Mai, 9.2%-efficient core-shell structured antimony selenide nanorod array solar cells. *Nat. Commun.* 2019, 10.
- [12] X. Wen, C. Chen, S. Lu, K. Li, R. Kondrotas, Y. Zhao, W. Chen, L. Gao, C. Wang,

- J. Zhang, G. Niu, J. Tang, Vapor transport deposition of antimony selenide thin film solar cells with 7.6% efficiency. *Nat. Commun.* 2018, 9, 2179.
- [13] L. Wang, D. B. Li, K. Li, C. Chen, H. X. Deng, L. Gao, Y. Zhao, F. Jiang, L. Li, F. Huang, Y. He, H. Song, G. Niu, J. Tang, Stable 6%-efficient Sb_2Se_3 solar cells with a ZnO buffer layer. *Nat. Energy* 2017, 2, 17046.
- [14] J. Tao, X. Hu, Y. Guo, J. Hong, K. Li, J. Jiang, S. Chen, C. Jing, F. Yue, P. Yang, C. Zhang, Z. Wu, J. Tang, J. Chu, Solution-processed SnO_2 interfacial layer for highly efficient Sb_2Se_3 thin film solar cells. *Nano Energy* 2019, 60, 802-809.
- [15] Y. C. Choi, T. N. Mandal, W. S. Yang, Y. H. Lee, S. H. Im, J. H. Noh, S. I. Seok, Sb_2Se_3 -Sensitized Inorganic-Organic Heterojunction Solar Cells Fabricated Using a Single-Source Precursor. *Angew. Chem., Int. Ed.* 2014, 53, 1329-1333.
- [16] Z. Yang, X. Wang, Y. Chen, Z. Zheng, Z. Chen, W. Xu, W. Liu, Y. Yang, J. Zhao, T. Chen, H. Zhu, Ultrafast self-trapping of photoexcited carriers sets the upper limit on antimony trisulfide photovoltaic devices. *Nat. Commun.* 2019, 10, 1-8.
- [17] C. Chen, K. H. Li, S. Y. Chen, L. Wang, S. C. Lu, Y. H. Liu, D. B. Li, H. S. Song, J. Tang, Efficiency Improvement of Sb_2Se_3 Solar Cells via Grain Boundary Inversion. *ACS Energy Lett.* 2018, 3, 2335-2341.
- [18] C. Ou, K. Shen, Z. Li, H. Zhu, T. Huang, Y. Mai, Bandgap tunable CdS:O as efficient electron buffer layer for high-performance Sb_2Se_3 thin film solar cells. *Sol. Energy Mater. Sol. Cells* 2019, 194, 47-53.
- [19] X. Wang, R. Tang, Y. Yin, H. Ju, S. a. Li, C. Zhu, T. Chen, Interfacial engineering for high efficiency solution processed Sb_2Se_3 solar cells. *Sol. Energy Mater. Sol. Cells* 2019, 189, 5-10.
- [20] M. Huang, P. Xu, D. Han, J. Tang, S. Chen, Complicated and Unconventional Defect Properties of the Quasi-One-Dimensional Photovoltaic Semiconductor Sb_2Se_3 . *ACS Appl. Mater. Interfaces* 2019, 11, 15564-15572.
- [21] X. Liu, X. Xiao, Y. Yang, D. J. Xue, D. B. Li, C. Chen, S. Lu, L. Gao, Y. He, M. C. Beard, G. Wang, S. Chen, J. Tang, Enhanced Sb_2Se_3 solar cell performance through theory-guided defect control. *Prog. Photovolt. Res. Appl.* 2017, 25, 861-870.
- [22] T. T. Ngo, S. Chavhan, I. Kosta, O. Miguel, H. J. Grande, R. Tena-Zaera, Electrodeposition of Antimony Selenide Thin Films and Application in Semiconductor Sensitized Solar Cells. *ACS Appl. Mater. Interfaces* 2014, 6, 2836-2841.
- [23] Y. Zhou, M. Y. Leng, Z. Xia, J. Zhong, H. B. Song, X. S. Liu, B. Yang, J. P. Zhang, J. Chen, K. H. Zhou, J. B. Han, Y. B. Cheng, J. Tang, Solution-Processed

- Antimony Selenide Heterojunction Solar Cells. *Adv. Energy Mater.* 2014, 4, 1301864.
- [24] D. Lee, J. Y. Cho, J. Heo, Improved efficiency of Sb₂Se₃/CdS thin-film solar cells: The effect of low-temperature pre-annealing of the absorbers. *Sol. Energy* 2018, 173, 1073-1079.
- [25] Y. Zhou, L. Wang, S. Chen, S. Qin, X. Liu, J. Chen, D. J. Xue, M. Luo, Y. Cao, C. Y. heng, E. H. Sargent, J. Tang, Thin-film Sb₂Se₃ photovoltaics with oriented one-dimensional ribbons and benign grain boundaries. *Nat. Photonics* 2015, 9, 409-415.
- [26] R. Tang, Z. H. Zheng, Z. H. Su, X. J. Li, Y. D. Wei, X. H. Zhang, Y. Q. Fu, J. T. Luo, P. Fan, G. X. Liang, Highly efficient and stable planar heterojunction solar cell based on sputtered and post-selenized Sb₂Se₃ thin film. *Nano Energy* 2019, 64, 103929.
- [27] O. Briot, M. Moret, C. Barbier, A. Tiberj, H. Peyre, A. Sagna, S. Contreras, Optimization of the properties of the molybdenum back contact deposited by radiofrequency sputtering for Cu(In_{1-x}Ga_x)Se₂ solar cells. *Sol. Energy Mater. Sol. Cells* 2018, 174, 418-422.
- [28] X. Li, D. Zhuang, N. Zhang, M. Zhao, X. Yu, P. Liu, Y. Wei, G. Ren, Achieving 11.95% efficient Cu₂ZnSnSe₄ solar cells fabricated by sputtering a Cu-Zn-Sn-Se quaternary compound target with a selenization process. *J. Mater. Chem. A* 2019, 7, 9948-9957.
- [29] C. Yan, J. Huang, K. Sun, S. Johnston, Y. Zhang, H. Sun, A. Pu, M. He, F. Liu, K. Eder, L. Yang, J. M. Cairney, N. J. Ekins-Daukes, Z. Hameiri, J. A. Stride, S. Chen, M. A. Green, X. Hao, Cu₂ZnSnS₄ solar cells with over 10% power conversion efficiency enabled by heterojunction heat treatment. *Nat. Energy* 2018, 3, 764-772.
- [30] G. Li, Z. Li, X. Liang, C. Guo, K. Shen, Y. Mai, Improvement in Sb₂Se₃ Solar Cell Efficiency through Band Alignment Engineering at the Buffer/Absorber Interface. *ACS Appl. Mater. Interfaces* 2019, 11, 828-834.
- [31] G. X. Liang, Z. H. Zheng, P. Fan, J. T. Luo, J. G. Hu, X. H. Zhang, H. L. Ma, B. Fan, Z. K. Luo, D. P. Zhang, Thermally induced structural evolution and performance of Sb₂Se₃ films and nanorods prepared by an easy sputtering method. *Sol. Energy Mater. Sol. Cells* 2018, 174, 263-270.
- [32] H. Guo, Z. Chen, X. Wang, Q. Cang, X. Jia, C. Ma, N. Yuan, J. Ding, Enhancement in the Efficiency of Sb₂Se₃ Thin-Film Solar Cells by Increasing Carrier Concentration and Inducing Columnar Growth of the Grains. *Sol. RRL* 2019, 3, 1970033.

- [33] Z. Li, X. Chen, H. Zhu, J. Chen, Y. Guo, C. Zhang, W. Zhang, X. Niu, Y. Mai, Sb₂Se₃ thin film solar cells in substrate configuration and the back contact selenization. *Sol. Energy Mater. Sol. Cells* 2017, 161, 190-196.
- [34] G. P. Joshi, N. S. Saxena, R. Mangal, A. Mishra, T. P. Sharma, Band gap determination of Ni-Zn ferrites. *Bull. Mater. Sci.* 2003, 26, 387-389.
- [35] L. Li, G. Li, T. Zhang, C. Lin, G. Wang, S. Dai, Q. Nie, Q. Jiao, Preparation and properties of Ge-Ga-La-S-AgI chalcogenide glass. *Ceram. Int.* 2017, 43, 4508-4512.
- [36] C. Chen, L. Wang, L. Gao, D. Nam, D. Li, K. Li, Y. Zhao, C. Ge, H. Cheong, H. Liu, H. Song, J. Tang, 6.5% Certified Efficiency Sb₂Se₃ Solar Cells Using PbS Colloidal Quantum Dot Film as Hole-Transporting Layer. *ACS Energy Lett.* 2017, 2, 2125-2132.
- [37] S G Haass, M Diethelm, M Werner, B Bissig, Y. E. Romanyuk, A N. Tiwari, 11.2% Efficient Solution Processed Kesterite Solar Cell with a Low Voltage Deficit. *Appl Energy Mater.* 2015, 5, 18.
- [38] M. Ishaq, H. Deng, S. Yuan, H. Zhang, J. Khan, U. Farooq, H. Song, J. Tang, Efficient Double Buffer Layer Sb₂(Se_xS_{1-x})₃ Thin Film Solar Cell Via Single Source Evaporation. *Sol. RRL* 2018, 2, 1800144.
- [39] W. Peng, X. Miao, V. Adinolfi, E. Alarousu, O. El Tall, A. H. Emwas, C. Zhao, G. Walters, J. Liu, O. Ouellette, J. Pan, B. Murali, E. H. Sargent, O. F. Mohammed, O. M. Bakr, Engineering of CH₃NH₃PbI₃ Perovskite Crystals by Alloying Large Organic Cations for Enhanced Thermal Stability and Transport Properties. *Angew. Chem., Int. Ed.* 2016, 55, 10686-10690.
- [40] K. Chen, P. Wu, W. Yang, R. Su, D. Luo, X. Yang, Y. Tu, R. Zhu, Q. Gong, Low-dimensional perovskite interlayer for highly efficient lead-free formamidinium tin iodide perovskite solar cells. *Nano Energy* 2018, 49, 411-418.
- [41] M. Luo, M. Y. Leng, X. S. Liu, J. Chen, C. Chen, S. K. Qin, J. Tang, Thermal evaporation and characterization of superstrate CdS/Sb₂Se₃ solar cells. *Appl. Phys. Lett.* 2014, 104, 173904.
- [42] X. B. Hu, J. H. Tao, G. E. Weng, J. C. Jiang, S. Q. Chen, Z. Q. Zhu, J. H. Chu, Investigation of electrically-active defects in Sb₂Se₃ thin-film solar cells with up to 5.91% efficiency via admittance spectroscopy. *Sol. Energy Mater. Sol. Cells* 2018, 186, 324-329.
- [43] J. Li, S. Kim, D. Nam, X. Liu, J. Kim, H. Cheong, W. Liu, H. Li, Y. Sun, Y. Zhang, Tailoring the defects and carrier density for beyond 10% efficient CZTSe thin film solar cells. *Sol. Energy Mater. Sol. Cells* 2017, 159, 447-455.

[44] X. Hu, J. Tao, Y. Wang, J. Xue, G. Weng, C. Zhang, S. Chen, Z. Zhu, J. Chu, 5.91%-efficient Sb_2Se_3 solar cells with a radio-frequency magnetron-sputtered CdS buffer layer. *Appl. Mater Today* 2019, 16, 367-374.